Oxygen Reduction Hot Paper

Deutsche Ausgabe: DOI: 10.1002/ange.201601568
Internationale Ausgabe: DOI: 10.1002/anie.201601568

Nitrogen-Rich Manganese Oxynitrides with Enhanced Catalytic Activity in the Oxygen Reduction Reaction

Akira Miura, Carolina Rosero-Navarro, Yuji Masubuchi, Mikio Higuchi, Shinichi Kikkawa, and Kiyoharu Tadanaga*

Abstract: *The catalytic activity of manganese oxynitrides in the oxygen reduction reaction (ORR) was investigated in alkaline solutions to clarify the effect of the incorporated nitrogen atoms on the ORR activity. These oxynitrides, with rock-salt-like structures with different nitrogen contents, were synthesized by reacting MnO, Mn_2O_3, or MnO_2 with molten $NaNH_2$ at 240–280 °C. The anion contents and the Mn valence states were determined by combustion analysis, powder X-ray diffraction, and X-ray absorption near-edge structure analysis. An increase in the nitrogen content of rock-salt-based manganese oxynitrides increases the valence of the manganese ions and reinforces the catalytic activity for the ORR in 1 M KOH solution. Nearly single-electron occupancy of the antibonding e_g states and highly covalent Mn−N bonding thus enhance the ORR activity of nitrogen-rich manganese oxynitrides.*

Catalysts for the oxygen reduction reaction (ORR) in alkaline solutions ($O_2 + 2H_2O + 4e^- \rightarrow 4OH^-$) are key materials for next-generation energy conversion and storage systems, including fuel cells and metal–air batteries, and efficient ORR catalysts are highly desirable.[1] Well-studied catalysts include perovskite oxides, such as $LaCoO_3$ and $LaMnO_3$, whose structure–activity relationships have been extensively explored.[1,2] Although the ORR is mechanistically complicated and influenced by the crystal structure, composition, electronic conductivity, surface adsorption behavior, and the incorporation of conductive additives,[1] structure–activity relationships provide rational guidelines for designing and understanding ORR catalysts.

Nitrides and related compounds have been studied as ORR catalysts. Binary and ternary nitrides, such as AlN, TiN, Cu_3N, and Cu_3PdN, are active catalysts of the ORR.[3] Oxynitrides, including ZrO_xN_y, MoO_xN_y, TaO_xN_y, and $CoMoO_xN_y$, also show catalytic activity.[4] Nonetheless, the correlations between structure and ORR activity have not been extensively studied, and the role of the amount of nitrogen in determining the catalytic activity has not been completely understood. Adjusting the amount of incorporated nitrogen is still challenging, mainly owing to the thermodynamic stability of the triple bond in molecular N_2. Furthermore, the nitrogen amount often has a significant effect on the crystal structure of the synthesized products,[5] thus complicating the interpretation of results.

Perovskite oxides contain metal–oxygen octahedra whose electronic structure can be schematically depicted by t_g and e_g states. Gasteiger, Shao-Horn, and co-workers have reported that nearly single-electron occupancy in e_g states (metal–oxygen antibonding orbitals) is beneficial for the electron transfer during the ORR cycle;[2d] a typical example of a compound with a single electron in the e_g orbital is $LaMnO_3$ with trivalent manganese. Furthermore, increasing the covalency of the metal–oxygen bonding in perovskite oxides is favorable for the ORR.[2c,d] As nitrogen has less electrons than oxygen and metal–nitrogen bonding is more covalent than metal–oxygen bonding, adjusting the nitrogen content can change the electronic structure and thus enhance the ORR activity. Oxynitrides with rock-salt-like structures contain metal–anion octahedra, and thus their electronic structures are similar to those of perovskite oxides. Both MnO and MnN_x ($x \geq 2/3$) adopt rock-salt-type structures,[6] and the Fermi level of stoichiometric MnN has been computationally predicted to be located near the boundary between the bonding and antibonding states.[7] Therefore, manganese oxynitrides with different anion contents are suitable motifs to examine the effect of the nitrogen content on the ORR activity. Herein, we examined the compositions, structures, valence states, and ORR activities of three manganese oxynitrides with rock-salt-type structures with different O/N anion ratios. Tuning the incorporated nitrogen amount in rock-salt-like structures was achieved by using the recently developed method for the low-temperature nitridation of manganese oxides with sodium amide.[8] The ORR activities of nitrogen-rich manganese oxynitrides were found to be higher than those of oxynitrides with a reduced nitrogen content and manganese monoxide.

The black manganese oxynitrides that were prepared from an alkaline molten salt and sodium amide by the above-mentioned method are highly stable towards bases, which is a prerequisite for ORR catalysts to be used in alkaline solution. The nitridation of Mn_2O_3, MnO_2, and MnO powders gave three different manganese oxynitrides, referred to as MnON(1), MnON(2), and MnON(3), respectively. Combustion analysis revealed that MnON(1) had the highest nitrogen content, followed by MnON(2) and MnON(3) (Table 1). Energy-dispersive X-ray spectroscopy showed peaks corresponding to nitrogen, oxygen, and manganese, with a small peak attributable to sodium; the Na/Mn ratio was semi-quantitatively estimated to be ≤ 0.01.

Scanning electron microscopy (SEM) images of the manganese oxynitride powders show aggregates of less than

[*] Dr. A. Miura, Dr. C. Rosero-Navarro, Dr. Y. Masubuchi, Dr. M. Higuchi, Prof. Dr. S. Kikkawa, Prof. Dr. K. Tadanaga
Faculty of Engineering, Hokkaido University
North 13 West 8, Kita-ku, Sapporo 060–0808 (Japan)
E-mail: amiura@eng.hokudai.ac.jp

Supporting information for this article can be found under: http://dx.doi.org/10.1002/anie.201601568.

 © 2016 Wiley-VCH Verlag GmbH & Co. KGaA, Weinheim

Table 1: Structural parameters of the manganese oxynitrides.

	MnON(1)	MnON(2)	MnON(3)
Mn/O/N molar ratio[a]	1:0.24:0.84	1:0.19:0.78	1:0.19:0.64
space group	*I*4/*mmm*	*I*4/*mmm*	*I*4/*mmm*
unit cell [nm]	$a = 0.298163(10)$	$a = 0.297592(12)$	$a = 0.297355(7)$
	$c = 0.414716(14)$	$c = 0.410434(16)$	$c = 1.21520(4)$
$Mn_4(O,N)_4$ cell[b] [nm]	$a = 0.421673(14)$	$a = 0.420866(16)$	$a = 0.420530(10)$
	$c = 0.414716(14)$	$c = 0.410434(16)$	$c = 0.405067(13)$
occupancy of the O,N sites[c]	0.998(6)	0.889(9)	0.779(1)
Na birnessite[d] [wt%]	1.5	2.6	2.5
$Mn(OH)_2$[d] [wt%]	0	0	1.5
R_{wp}[e] [%]	8.95	11.9	14.2
S[f]	1.20	1.67	1.65
Mn valence[g]	3.0	2.8	2.4

[a] Determined by combustion analysis; calculated from the measured values for N and O and the residuals for Mn. [b] The $Mn_4(O,N)_4$ unit cells were visualized for comparison of their lattice parameters (Figure 2). [c] Derived by Rietveld analysis assuming that anion sites are occupied only by nitrogen and cation sites are fully occupied by manganese. The occupancy quoted for MnON(3) is the total occupancy of the two anion sites. [d] Derived from Rietveld analysis: $Na_{0.364}MnO_2(H_2O)_{0.544}$ (ICSD No. 96606), $Mn(OH)_2$ (ICSD No. 23591). [e] $R_{wp} = \left\{ \frac{\sum_{i=1}^{N} w_i [y_i - f_i(x)]^2}{\sum_{i=1}^{N} x_i y_i^2} \right\}^{1/2}$.[11] [f] $S = \left\{ \frac{\sum_{i=1}^{N} w_i [y_i - f_i(x)]^2}{(N-n)} \right\}^{1/2}$.[11] [g] Estimated values from the Mn K-edge X-ray absorption spectrum.

a few micrometers in size (Figure 1 a–d). The sizes of the primary particles were estimated to be approximately 30–100 nm for MnON(1), 80–150 nm for MnON(2), and 50–300 nm for MnON(3) and MnO according to a transmission electron microscopy (TEM) analysis. Electron diffraction gave diffraction spots that could be assigned to strong diffractions of rock salt structures.

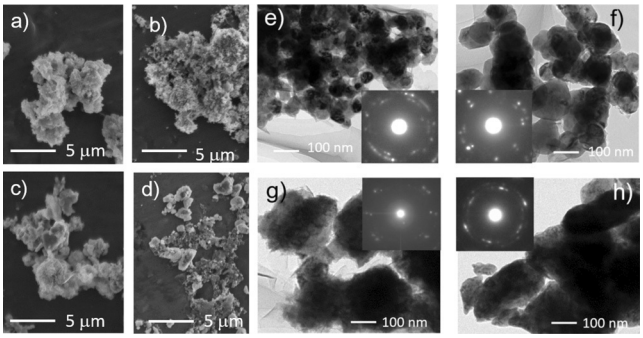

Figure 1. SEM images of a) MnON(1), b) MnON(2), c) MnON(3), and d) MnO. TEM and electron-diffraction images of e) MnON(1), f) MnON(2), g) MnON(3), and h) MnO.

The X-ray diffraction (XRD) patterns of the manganese oxynitrides are shown in Figure 2, and the Rietveld refinement results are summarized in Table 1. Major diffraction peaks characteristic of rock salt structures and minor peaks attributable to sodium birnessite and $Mn(OH)_2$ were detected. The oxynitrides have tetragonal structures featuring Mn/(O,N) octahedra, with the *c* axis being slightly shorter than the *a* and *b* axes. MnON(3), which has the lowest nitrogen content, consists of a superlattice with ordered anion vacancies with a tripled *c* axis compared to the rock salt structure; weak superlattice spots were observed by electron diffraction (Supporting Information, Figure S1). For comparison, the unit cell of $Mn_4(O,N)_4$ was regarded to be similar to the unit cell of cubic rock salt. The increase in nitrogen content from MnON(3) to MnON(1) shifted the diffraction peaks toward lower angles, which corresponds to an increase in the lattice parameters. For the three manganese oxynitrides, the peaks also showed different relative intensities. The freely refined occupancies of the anion sites by Rietveld refinement suggest that the increase in nitrogen content leads to an increase in the occupancy of the anion sites. Figure 3 shows the manganese K-edge X-ray absorption spectrum. The absorption edge is shifted towards higher energies with increasing nitrogen content, suggesting an increased Mn valence from 2.4 to 3.0 in the synthesized oxynitride powders. The surfaces of the manganese oxynitrides were examined by X-ray photoelectron spectroscopy (XPS). For the three manganese oxynitrides, the O and N signals were detected at approximately 529.5 and 395.8 eV, respectively, suggesting Mn–O and Mn–N bonding (Figure S2).[9] The oxygen signal has a tail towards higher energies, implying the presence of OH^- species on the surface.[10] Strong nitrogen signals were detected for MnON(1) and MnON(2) compared with the relatively weak signal for MnON(3).

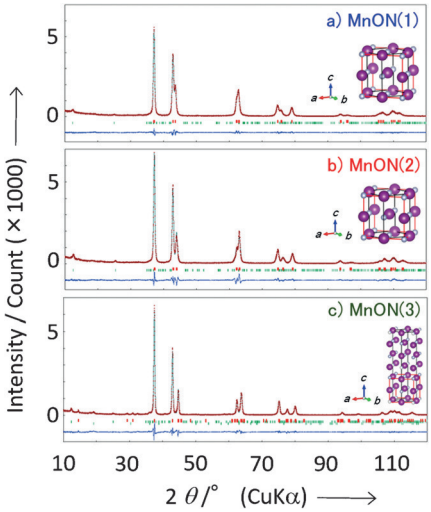

Figure 2. Rietveld profiles of the X-ray diffraction patterns of a) MnON(1), b) MnON(2), and c) MnON(3). Bars (red: manganese oxynitrides; green: Na birnessite and $Mn(OH)_2$) indicate the calculated positions of the Bragg peaks, and the bottom lines (blue) represent residuals. Insets: Structural models of the cells: Large and small spheres represent Mn and O/N sites, respectively. Black and red lines represent the unit-cell boundaries and the $Mn_4(O,N)_4$ cell, respectively.

© 2016 Wiley-VCH Verlag GmbH & Co. KGaA, Weinheim

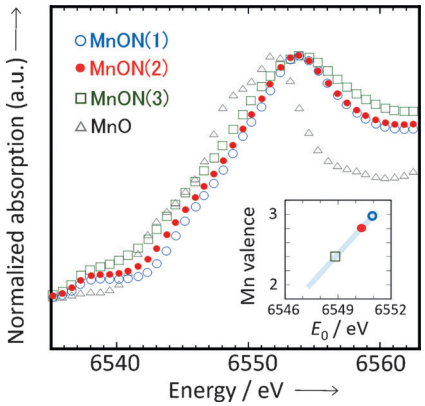

Figure 3. Mn K-edge X-ray absorption spectra of the manganese oxynitrides. Inset: Calibration line for the estimation of the Mn valence from the inflection points (E_0) using MnO and Mn_2O_3 standards.

The anion occupancies and Mn valence states calculated from chemical analysis show the same qualitative trends as those derived from XRD and X-ray absorption; an increase in nitrogen content from MnON(3) to MnON(1) leads to an increase in the anion site occupancy and correlates with the increased Mn valence. The increase in anion site occupancy by increasing the nitrogen content leads to an elongation of the lattice parameters of the rock-salt-based structures. Nonetheless, the values for the anion occupancy and Mn valence calculated from the chemical analysis deviate by approximately 0.1 from those derived from XRD and X-ray absorption. These deviations can be attributed to impurity phase(s), the surface layer analyzed by XPS, possible cation vacancies, as well as the error in the Mn valence estimated using oxide standards. The relationship between the nitrogen content, the anion vacancy, and the lattice parameters is similar to that reported for manganese nitrides: $Mn_6N_{5.26}$ (a = 0.42193(1) nm, c = 0.41287(1) nm) and Mn_3N_2 (a = 0.42193 nm, c = 1.2124(1) nm).[6] Small differences in the lattice parameters of manganese oxynitrides and reported manganese nitrides can be related to slightly deviating nitrogen and oxygen amounts.

The ORR activities of the three manganese oxynitrides in an O_2-saturated alkaline aqueous solution were examined by linear sweep polarization (Figure 4). The increasing nitrogen content in the rock-salt-based structures from MnO through MnON(3) to MnON(2) shifts the onset of the ORR towards higher potentials (Figure 4a). MnON(1) and MnON(2) show the highest onsets for ORR activity. These onsets are approximately 0.07 eV lower in energy than that of Pt/C, and close to that of Mn_2O_3 (Figure 4a, inset). In argon-saturated KOH solution, a current density of less than $-0.1\ mA\,cm^{-2}$ was detected for MnON(2), suggesting that the ORR takes place in O_2-saturated solution. Kouteky–Levich plots[1] of the current at −0.4 V at rotation speeds of 400–2500 rpm (Figure 4b) are linear, and the number of electrons estimated from these slopes is 3.2 for MnON(1), 3.6 for MnON(2), 2.8 for MnON(3), and 2.4 for MnO. Therefore, an increased nitrogen content in rock-salt-type oxynitrides reduces the overpotential of the ORR and enhances the (pseudo-)four electron reaction.

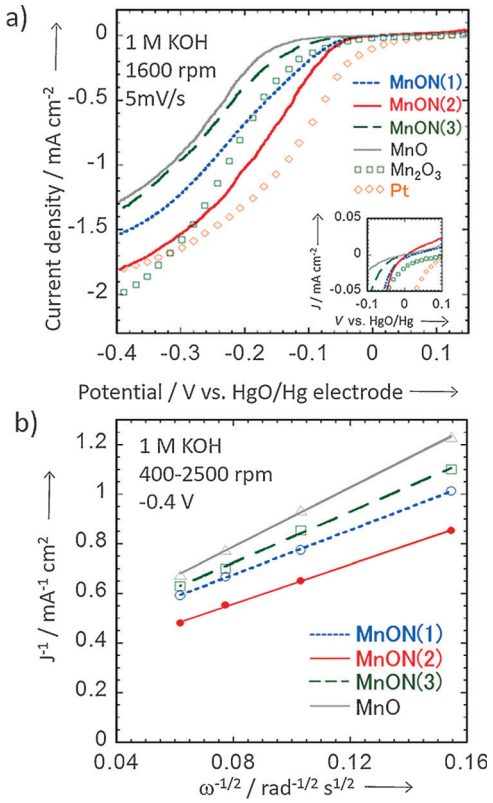

Figure 4. a) Linear-sweep polarization curves of MnON(1), MnON(2), MnON(3), and MnO recorded with a rotating disc electrode in O_2-saturated 1 M KOH solution at a sweep rate of 5 $mV\,s^{-1}$. The polarization curves of Pt/C and Mn_2O_3 are shown for comparison. b) Kouteky–Levich plots at −0.4 eV and 400–2500 rpm.

The structure–activity relationships of manganese oxynitrides can be rationalized by considering the octahedral motif as proposed for perovskite oxides. In perovskite oxides with metal–oxygen octahedra, nearly single-electron occupancy in the antibonding e_g states and more covalent metal–oxygen bonding are beneficial in terms of the onset potential for the ORR current.[2d] The manganese valences in nitrogen-rich MnON(1) and MnON(2), which show the highest onset potentials, are close to three, thus Mn/(O,N) octahedra with approximately one electron in the antibonding e_g states are expected. Although the surface area of the aggregated oxynitride powders would affect the magnitude of the current density of the ORR, it would have a relatively small influence on the onset potential. Thus the comparison of manganese oxynitrides and perovskite oxides suggests that the highest onset potential of the ORR currents in MnON(1) and MnON(2) can be explained by the presence of approximately one electron in the antibonding e_g state (Figure S3). Moreover, the high covalency of the Mn–N bonding in nitrogen-rich Mn/(O,N) octahedra can enhance the activity by increasing the energy of the antibonding e_g state, increasing the driving force for the ORR. First-principles calculations support the expected electronic structures; the antibonding states of MnN contained less electrons than those of MnO, and the Fermi level of MnN is located at a higher energy than that of MnO (Figure S3). This simple octahedral model does not consider possible cation vacancies, the distribution of the

 © 2016 Wiley-VCH Verlag GmbH & Co. KGaA, Weinheim

nitrogen and oxygen atoms and the vacancies in the anion sites, and the distortion of the octahedra. The effect of the morphology and surface composition of oxynitride powders on the ORR activity needs further investigation. Nonetheless, using the octahedron model, the maximum onset voltage of the ORR current can be explained by approximately one electron in the e_g states and enhanced covalency in both manganese oxynitrides and perovskite oxides. Therefore, the overall similarity in electron count, covalency, and ORR activity between rock-salt-type manganese oxynitrides and perovskite oxides suggests that the tuning of the N/O ratios in octahedral coordination with approximately one electron in the e_g states can enhance the ORR catalytic activity.

In summary, low-temperature $NaNH_2$ nitridation of manganese oxides led to the formation of oxynitrides with different nitrogen contents depending on the oxide used. A higher nitrogen content led to increases in the lattice parameters, the occupancy of the anion sites, and the valence of manganese, and enhanced the catalytic activity in the ORR. Nearly single-electron occupancy of the e_g states and highly covalent bonding in the Mn/(O,N) octahedra provide a basis for this enhancement. This work thus proposes a strategy for enhancing ORR activities by optimizing the amount of nitrogen and oxygen octahedrally coordinated to a metal.

Experimental Section

The manganese oxynitrides were synthesized according to a procedure for low-temperature nitridation using sodium amide.[8] The starting oxides MnO (Strem Chemicals, 99%), Mn_2O_3 (Aldrich, 99%), and MnO_2 (Wako, 99.5%) were ground into fine powder with a planetary ball mill at 300 rpm for 90 min in an Ar-filled glove box. The corresponding powdered oxide (0.30–0.40 g) was mixed with $NaNH_2$ powder (2.0 g, Aldrich, 95%) and put in a steel crucible in a glove box. The crucible was placed in a steel autoclave, which was tightly closed and heated at 240–280 °C for 36 h outside the glove box. After the autoclave had been cooled to room temperature, the crucible was removed and an ethanol/water mixture was added to remove $NaNH_2$ and byproducts. The black precipitates were collected by filtration and further washed with ethanol/water. **Caution!** Sodium amide powder is highly sensitive to air and moisture, flammable, and can cause burns. Removing $NaNH_2$ with water/ethanol should be performed with great care.

The morphology of the powdered samples was determined by SEM (JEOL, JSM-6510LA) and TEM (JEOL, JEM-2010). The structures of the synthesized oxynitrides were examined using powder X-ray diffraction with CuKα radiation (Rigaku, RINT-2000). Rietveld analysis was performed with the RIETAN-FP package,[11] and crystal structures were drawn using VESTA.[12] The oxygen and nitrogen contents of the samples were determined with an oxygen/nitrogen combustion analyzer (Horiba, EMGA-620W). The sodium content was semi-quantitatively measured by energy-dispersive spectroscopy in combination with SEM. The surfaces of the powders were examined by XPS (JEOL, JPS-9200). The binding energies were corrected by reference to free carbon (284.6 eV). The Mn K-edge XANES spectrum was measured in transmission mode at the BL-9A beamline of the Photon Factory of the High Energy Accelerator Research Organization (KEK, Tsukuba). A small amount of the sample powder was mixed with boron nitride powder (Kojyundo Chem., 99%) and then pelletized for XANES measurements.

Electrochemical measurements were performed using a rotating disk electrode in oxygen- or argon-saturated 1M KOH aqueous solutions. Thin-film electrodes on glassy carbon disks were prepared by five-times-repeated pipetting and drying of 1.5 μL of the suspension. The suspension was produced by ultrasonication of a mixture of the oxynitride (2 mg), Vulcan carbon (2 mg), and ionomer (Tokuyama Corporation, 60 μL) in ethanol (540 μL). All potentials were referenced to the HgO/Hg electrode in 1M aq. KOH. The experiments with finely powdered MnO and Mn_2O_3 and Pt/C (ETEK 10 wt% Pt) were performed analogously.

The non-polarized density of states (DOS) and crystal orbital Hamilton populations (COHP)[13] were calculated with the Vienna ab initio Simulation Package[14] and the LOBSTER code.[15] The generalized gradient approximation of PBE type and the projector-augmented wave method were used.[16] Stoichiometric MnO and MnN with cubic rock salt structure without vacancies were utilized as the initial models, and their lattice parameters and atom positions were optimized. A Monkhorst–Pack k-point grid of $12 \times 12 \times 12$ points was used.[17]

Acknowledgements

We thank Takashi Kubota for help with the ORR measurements, Kouta Tateno for help with the combustion and XANES analyses, Prof. Yoshitaka Aoki for discussions on the ORR, Dr. Yongming Wang for TEM analysis, and Tokuyama corporation for providing the ionomer. The SEM, TEM, and XPS analyses were carried out at the Joint-use Facilities: Laboratory of Nano-Micro Material Analysis & Laboratory of XPS analysis, Hokkaido University. The XANES experiments were performed after approval of Proposal 2015G602 by the Photon Factory Advisory Committee.

Keywords: manganese · nitrides · oxygen reduction · oxynitrides

How to cite: *Angew. Chem. Int. Ed.* **2016**, *55*, 7963–7967
Angew. Chem. **2016**, *128*, 8095–8099

[1] a) X. Ge, A. Sumboja, D. Wuu, T. An, B. Li, F. W. T. Goh, T. S. A. Hor, Y. Zong, Z. Liu, *ACS Catal.* **2015**, *5*, 4643–4667; b) W. T. Hong, M. Risch, K. A. Stoerzinger, A. Grimaud, J. Suntivich, Y. Shao-Horn, *Energy Environ. Sci.* **2015**, *8*, 1404–1427.

[2] a) D. B. Meadowcroft, *Nature* **1970**, *226*, 847–848; b) Y. Matsumoto, H. Yoneyama, H. Tamura, *J. Electroanal. Chem. Interfacial Electrochem.* **1977**, *83*, 237–243; c) Y. Matsumoto, H. Yoneyama, H. Tamura, *J. Electroanal. Chem. Interfacial Electrochem.* **1977**, *79*, 319–326; d) J. Suntivich, H. A. Gasteiger, N. Yabuuchi, H. Nakanishi, J. B. Goodenough, Y. Shao-Horn, *Nat. Chem.* **2011**, *3*, 546–550.

[3] a) D. D. Vaughn II, J. Araujo, P. Meduri, J. F. Callejas, M. A. Hickner, R. E. Schaak, *Chem. Mater.* **2014**, *26*, 6226–6232; b) R. Ohnishi, M. Katayama, D. Cha, K. Takanabe, J. Kubota, K. Domen, *J. Electrochem. Soc.* **2013**, *160*, F501–F506; c) Z. Jin, P. Li, D. Xiao, *Sci. Rep.* **2014**, *4*, 6712; d) M. Lei, J. Wang, J. R. Li, Y. G. Wang, H. L. Tang, W. J. Wang, *Sci. Rep.* **2014**, *4*, 6013; e) A. Miura, M. E. Tague, J. M. Gregoire, X.-D. Wen, R. B. van Dover, H. D. Abruña, F. J. DiSalvo, *Chem. Mater.* **2010**, *22*, 3451–3456; f) H. Wu, W. Chen, *J. Am. Chem. Soc.* **2011**, *133*, 15236–15239.

[4] a) C. Pozo-Gonzalo, O. Kartachova, A. A. J. Torriero, P. C. Howlett, A. M. Glushenkov, D. M. Fabijanic, Y. Chen, S. Poissonnet, M. Forsyth, *Electrochim. Acta* **2013**, *103*, 151–160; b) S. Doi, A. Ishihara, S. Mitsushima, N. Kamiya, K.-i. Ota, *J. Electrochem. Soc.* **2007**, *154*, B362; c) A. Seifitokaldani, M. Perrier, O. Savadogo, *J. New Mater. Electrochem. Syst.* **2014**, *17*, 055–065; d) B. Cao, G. M. Veith, R. E. Diaz, J. Liu, E. A. Stach,

 © 2016 Wiley-VCH Verlag GmbH & Co. KGaA, Weinheim

R. R. Adzic, P. G. Khalifah, *Angew. Chem. Int. Ed.* **2013**, *52*, 10753 – 10757; *Angew. Chem.* **2013**, *125*, 10953 – 10957.
[5] A. Miura, K. Tadanaga, E. Magome, C. Moriyoshi, Y. Kuroiwa, T. Takahiro, N. Kumada, *J. Solid State Chem.* **2015**, *229*, 272 – 277.
[6] A. Leineweber, R. Niewa, H. Jacobs, W. Kockelmann, *J. Mater. Chem.* **2000**, *10*, 2827 – 2834.
[7] B. Eck, R. Dronskowski, M. Takahashi, S. Kikkawa, *J. Mater. Chem.* **1999**, *9*, 1527 – 1537.
[8] a) A. Miura, T. Takei, N. Kumada, *Cryst. Growth Des.* **2012**, *12*, 4545 – 4547; b) A. Miura, T. Takei, N. Kumada, *Inorg. Chem.* **2013**, *52*, 11787 – 11791; c) A. Miura, T. Takei, N. Kumada, *J. Asian Ceram. Soc.* **2014**, *2*, 326 – 328.
[9] a) M. A. Stranick, *Surf. Sci. Spectra* **1999**, *6*, 39 – 46; b) I. Bertóti, *Surf. Coat. Technol.* **2002**, *151 – 152*, 194 – 203.
[10] J. Torres, C. C. Perry, S. J. Bransfield, D. H. Fairbrother, *J. Phys. Chem. B* **2003**, *107*, 5558 – 5567.
[11] F. Izumi, K. Momma, *Solid State Phenom.* **2007**, *130*, 15 – 20.
[12] K. Momma, F. Izumi, *J. Appl. Crystallogr.* **2008**, *41*, 653 – 658.
[13] R. Dronskowski, P. E. Bloechl, *J. Phys. Chem.* **1993**, *97*, 8617 – 8624.
[14] G. Kresse, J. Hafner, *Phys. Rev. B* **1993**, *47*, 558 – 561.
[15] a) V. L. Deringer, A. L. Tchougréeff, R. Dronskowski, *J. Phys. Chem. A* **2011**, *115*, 5461 – 5466; b) S. Maintz, V. L. Deringer, A. L. Tchougreeff, R. Dronskowski, *J. Comput. Chem.* **2016**, *37*, 1030 – 1035.
[16] a) P. E. Blöchl, *Phys. Rev. B* **1994**, *50*, 17953 – 17979; b) G. Kresse, D. Joubert, *Phys. Rev. B* **1999**, *59*, 1758 – 1775; c) J. P. Perdew, J. A. Chevary, S. H. Vosko, K. A. Jackson, M. R. Pederson, D. J. Singh, C. Fiolhais, *Phys. Rev. B* **1992**, *46*, 6671 – 6687.
[17] H. J. Monkhorst, J. D. Pack, *Phys. Rev. B* **1976**, *13*, 5188 – 5192.

Received: February 13, 2016
Revised: April 8, 2016
Published online: May 19, 2016

 © 2016 Wiley-VCH Verlag GmbH & Co. KGaA, Weinheim